

# The impact of chemical differentiation of white dwarfs on thermonuclear supernovae

E. Bravo<sup>1</sup>, L. G. Althaus<sup>2,3,4</sup>, E. García-Berro<sup>2,5</sup>, and I. Domínguez<sup>6</sup>

<sup>1</sup> Departament de Física i Enginyeria Nuclear, Universitat Politècnica de Catalunya, c/Comte d'Urgell 187, 08036 Barcelona, Spain  
e-mail: eduardo.bravo@upc.edu

<sup>2</sup> Departament de Física Aplicada, Universitat Politècnica de Catalunya, c/Esteve Terrades 5, 08860 Castelldefels, Spain  
e-mail: garcia@fa.upc.edu

<sup>3</sup> Facultad de Ciencias Astronómicas y Geofísicas, Universidad Nacional de La Plata, Paseo del Bosque s/n, 1900 La Plata, Argentina  
e-mail: althaus@fcaglp.fcaglp.unlp.edu.ar

<sup>4</sup> Instituto de Astrofísica de La Plata (CCT La Plata), CONIC ET, 1900 La Plata, Argentina

<sup>5</sup> Institut d'Estudis Espacials de Catalunya, Ed. Nexus-201, c/Gran Capita 2–4, 08034 Barcelona, Spain

<sup>6</sup> Departamento de Física Teórica y del Cosmos, Universidad de Granada, 18071 Granada, Spain

Received 30 July 2010 / Accepted 24 October 2010

## ABSTRACT

**Aims.** Gravitational settling of  $^{22}\text{Ne}$  in cooling white dwarfs can affect the outcome of thermonuclear supernovae. We investigate how the supernova energetics and nucleosynthesis are in turn influenced by this process. We use realistic chemical profiles derived from state-of-the-art white dwarf cooling sequences. The cooling sequences provide a link between the white dwarf chemical structure and the age of the supernova progenitor system.

**Methods.** The cooling sequence of a  $1 M_{\odot}$  white dwarf was computed until freezing using an up-to-date stellar evolutionary code. We computed explosions of both Chandrasekhar mass and sub-Chandrasekhar mass white dwarfs, assuming spherical symmetry and neglecting convective mixing during the pre-supernova carbon simmering phase to maximize the effects of chemical separation.

**Results.** Neither gravitational settling of  $^{22}\text{Ne}$  nor chemical differentiation of  $^{12}\text{C}$  and  $^{16}\text{O}$  have an appreciable impact on the properties of type Ia supernovae, unless there is a direct dependence of the flame properties (density of transition from deflagration to detonation) on the chemical composition. At a fixed transition density, the maximum variation in the supernova magnitude obtained from progenitors of different ages is  $\sim 0.06$  mag, and even assuming an unrealistically large diffusion coefficient of  $^{22}\text{Ne}$  it would be less than  $\sim 0.09$  mag. However, if the transition density depends on the chemical composition (all other things being equal) the oldest SNIa can be as much as 0.4 mag brighter than the youngest ones (in our models the age difference is 7.4 Gyr). In addition, our results show that  $^{22}\text{Ne}$  sedimentation cannot be invoked to account for the formation of a central core of stable neutron-rich Fe-group nuclei in the ejecta of sub-Chandrasekhar models, as required by observations of type Ia supernovae.

**Key words.** diffusion – distance scale – stars: interiors – supernovae: general – stars: evolution – white dwarfs

## 1. Introduction

Thermonuclear explosions of accreting white dwarfs are thought to be the origin of several of the most violent phenomena known: type Ia supernovae (SNIa) (Hoyle & Fowler 1960; Branch et al. 1995; Hillebrandt & Niemeyer 2000; Röpke 2006), .Ia supernovae (Bildsten et al. 2007), and even some type Ib supernovae (Perets et al. 2010). The discovery of the accelerated expansion of the Universe (Riess et al. 1998; Perlmutter et al. 1999) has put SNIa at the center of attention of cosmologists, as a complete knowledge of any systematics affecting SNIa luminosity is necessary to achieve the precision required to measure the equation of state of dark matter (see, e.g. Tonry 2005).

One of the most intriguing systematics concerning SNIa variability is the correlation suggested by the observations between supernova brightness and progenitor age, the so-called “age effect” (there is another type of age effect that correlates the SNIa rate with age, see for instance Nomoto et al. 2000). The luminosity of SNIa is related to the morphological types of their host galaxies: brighter SNIa tend to occur in spiral galaxies with younger stellar populations, while most of the fainter events occur preferentially in early-type galaxies with relatively older

stars (Hamuy et al. 1996, 2000; Wang et al. 2006). This observational finding implies that the age difference of the progenitors is one of the origins of SNIa diversities. The age effect may have its origin in either the intrinsic dependence of the observational properties of individual supernovae on the age of their progenitors (this could be called a pure age effect) or the occurrence of different channels leading to SNIa, each one characterized by slightly different properties and time histories (e.g. white dwarf mergers versus single degenerate progenitors), or even in observational biases. In this work, we focus on a possible pure age effect caused by the chemical differentiation that occurs during white dwarf cooling prior to the supernova event.

Observational constraints on the nature of the age effect come from statistical studies of the properties of large numbers of SNIa in different environments. Gallagher et al. (2008) found a strong correlation suggesting that SNIa in galaxies whose population is older than 5 Gyr are  $\sim 1$  mag fainter at maximum than those found in galaxies with younger populations. They concluded that the time since progenitor formation primarily determines the production of  $^{56}\text{Ni}$ , the main radioactive nuclide powering the light curve. A similar conclusion was obtained by Howell et al. (2009). Neill et al. (2009) pointed out what appears

to be a threshold average population age of 3 Gyr above which a host is less likely to produce SNIa with  $^{56}\text{Ni}$  masses greater than  $\sim 0.5 M_{\odot}$ . Below this age threshold, there appears to be little correlation between  $^{56}\text{Ni}$  mass and host age. These findings tightly constrain the possible origin of the age effect. For instance, Krueger et al. (2010) attributed the luminosity-age correlation to an increase in the central density of the white dwarf prior to the SNIa explosion, during the accretion phase of the progenitor system. However, they only explored cooling times below  $\sim 1$  Gyr, which are much less than the threshold suggested by Neill et al. (2009).

Timmes et al. (2003) and Tonry (2005) argued that sedimentation of  $^{22}\text{Ne}$  over a timescale of several (up to  $\sim 7$ – $8$ ) Gyr provides a natural time-dependent mechanism modulating the luminosity of a white dwarf explosion. The sequence of events can be divided into three phases. First, the primary component of a binary system evolves into a white dwarf. For the range of white dwarf progenitor masses, the timescale of the first phase is on the order of  $\lesssim 1$  Gyr. Second, there is a variable period of time during which the secondary remains in the main-sequence and the white dwarf cools and acquires a (perhaps partially) chemically differentiated structure. Third, there is an accretion phase during which the white dwarf grows in mass and increases its central density. At the accretion rates necessary to allow a SNIa explosion, the duration of this last phase can be much less than 1 Gyr. For nearby SNIa, which presumably sample a range of progenitor ages, the sedimentation of  $^{22}\text{Ne}$  during the second phase might introduce a larger variability of luminosity than for SNIa exploding at higher redshift, for instance  $z \sim 1$ .

From the theoretical point of view, there is a long history of calculations that have tried to unravel the influence of  $^{22}\text{Ne}$  sedimentation on the physics of SNIa (e.g. Bravo et al. 1992). Bildsten & Hall (2001) proposed to use the production of  $^{54}\text{Fe}$  in SNIa as an indirect test of the sedimentation of  $^{22}\text{Ne}$ . Piro & Chang (2008) analyzed the impact of  $^{22}\text{Ne}$  sedimentation on the size of the convective zone during the last stages of carbon simmering, which set the initial conditions for a SNIa explosion (see also Piro & Bildsten 2008). They claimed that to have an appreciable effect it would be necessary for all the  $^{22}\text{Ne}$  to diffuse into the convective core prior to carbon ignition. In their modeling of sub-Chandrasekhar white dwarf explosions, Sim et al. (2010) had to resort to a hypothetical gravitational settling of  $^{22}\text{Ne}$  to reproduce the central concentration of neutron-rich isotopes inferred from observations of SNIa.

García-Berro et al. (2008), Althaus et al. (2010), Renedo et al. (2010), and García-Berro et al. (2010) computed realistic white dwarf cooling sequences with updated physics, in which the evolution was followed simultaneously with the several possible chemical differentiation processes: gravitational settling of  $^{22}\text{Ne}$  during the liquid phase and chemical separation during the liquid-solid phase transition. It is, thus, interesting to know the consequences of these state-of-the-art white dwarf evolutionary calculations on the outcome of the thermonuclear explosions of these objects, to see whether they meet the expectations raised by the above-mentioned models of SNIa. The plan of the paper is as follows. In the next section, we briefly outline the chemical differentiation processes that take place during white dwarf cooling. The chemical profiles obtained at both the beginning and the end of the cooling process are used as input models for the thermonuclear supernova code. In Sect. 3, we report the results of the explosion of a Chandrasekhar-mass white dwarf, and the sensitivity of the supernova properties to the age of the progenitor. Section 4 is devoted to evaluating the impact of the chemical profiles on sub-Chandrasekhar white dwarf explosions,

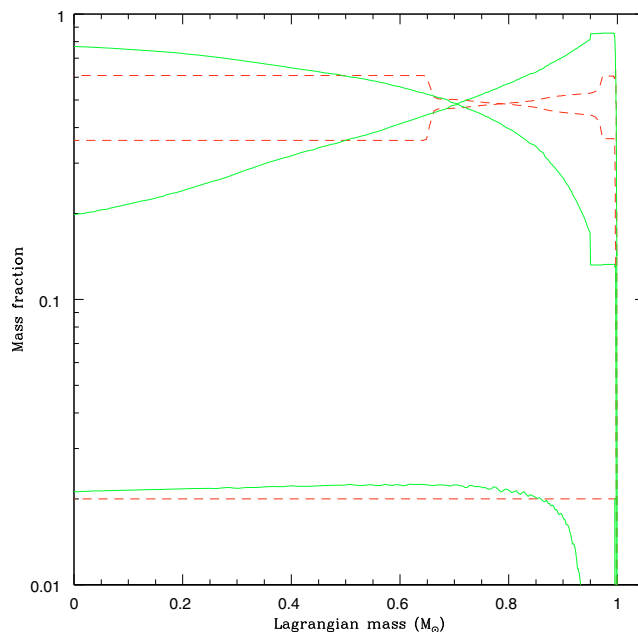


**Fig. 1.** Chemical profile of the white dwarf at the beginning of the cooling process (red) and the the end of crystallization (green). The three abundances shown for each model belong (from top to bottom at  $M = 0$ ) to:  $^{16}\text{O}$ ,  $^{12}\text{C}$ , and  $^{22}\text{Ne}$ . The mass fraction of  $^{12}\text{C}$  in the outermost layer is 0.61 (red line) and 0.86 (green line).

where we account for their possible impact on the formation of a carbon detonation at the top of the carbon-oxygen core as a consequence of a helium detonation (the double-detonation scenario for sub-Chandrasekhar white dwarfs). Finally, in Sect. 5 we summarize our major findings and draw our conclusions.

## 2. Chemical differentiation during white dwarf cooling

The white dwarf evolutionary models used in this work were extracted from the full evolution of a  $1.0 M_{\odot}$  cooling sequence computed with the LPCODE stellar evolutionary code (see Althaus et al. 2010, for details). Particular attention was devoted to the treatment of the abundance changes resulting from the various physical processes acting during the cooling phase, namely element diffusion in the outer layers, carbon-oxygen phase separation upon core crystallization, and the slow  $^{22}\text{Ne}$  sedimentation in the liquid regions. The last process is particularly relevant to the present work.  $^{22}\text{Ne}$  sedimentation towards the center of the white dwarf results from an imbalance between gravitational and electrical forces caused by their being two extra neutrons in the  $^{22}\text{Ne}$  nucleus relative to  $A_i = 2Z_i$  nuclei (Bravo et al. 1992; Deloye & Bildsten 2002; García-Berro et al. 2008). In our simulations, time-dependent  $^{22}\text{Ne}$  sedimentation was treated in a self-consistent way with the white dwarf evolution, and we refer the reader to Althaus et al. (2010) for details. In particular, for the liquid regions, we adopt the diffusion coefficient  $D = 7.3 \times 10^{-7} T / \rho^{1/2} Z \Gamma^{1/3} \text{ cm}^2 \text{ s}^{-1}$  (see Deloye & Bildsten 2002). The chemical stratification of our starting white dwarf configuration at the beginning of the cooling track (depicted in Fig. 1) is the result of the complete evolution of an initially  $5.0 M_{\odot}$  model star evolved from the zero-age main sequence, through the core hydrogen-burning phase, the helium burning phase, and the thermally pulsing asymptotic giant branch phase,

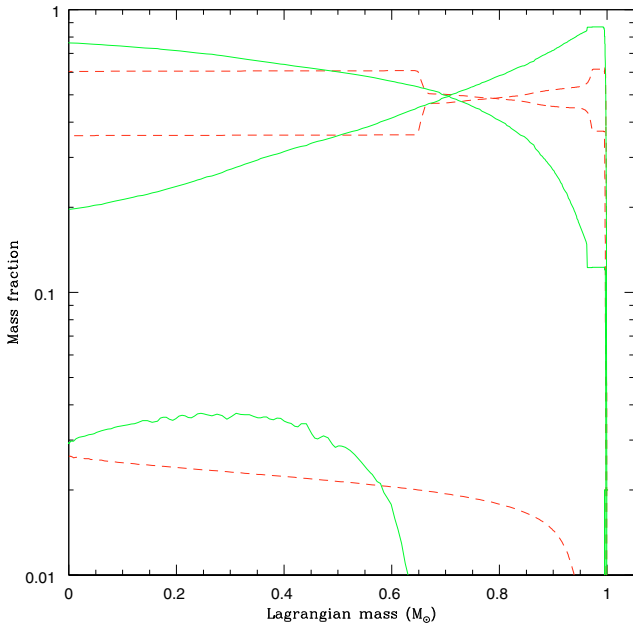


**Fig. 2.** Same as Fig. 1 but for a diffusion coefficient artificially increased by factor of five.

to the white dwarf stage (see [Renado et al. 2010](#)). The initial mass abundance of  $^{22}\text{Ne}$  in the core is 0.02 (by mass).

Noticeable changes in the chemical abundance distribution take place as the white dwarf evolves. During the evolutionary stages prior to core crystallization, abundance changes in the white dwarf core result from  $^{22}\text{Ne}$  sedimentation. As demonstrated by [Deloye & Bildsten \(2002\)](#) and [García-Berro et al. \(2008\)](#),  $^{22}\text{Ne}$  sedimentation is a very slow process that influences the evolution of white dwarfs only after long enough times have elapsed. During the evolutionary stages where most of the white dwarf remains in a liquid state, this process causes a strong depletion of  $^{22}\text{Ne}$  in the outer region of the core, and an enhancement of its abundance in the central regions of the star. This can be noted from Fig. 1. When most of the white dwarf has crystallized – at  $\approx 6$  Gyr – there remains no trace of  $^{22}\text{Ne}$  in the outer parts of the core. This is more noticeable in the case of a more efficient diffusion, as shown in Fig. 2. If we multiply the (rather uncertain) diffusion coefficient by a factor of 5, we indeed find that  $^{22}\text{Ne}$  diffuses so deep into the core that no trace of this element is found in layers even as deep as  $0.4 M_{\odot}$  below the stellar surface.

Finally, we note that the carbon-oxygen distribution becomes strongly modified by the time the star has ended its crystallization process. This is a result of the carbon-oxygen phase separation and the induced mixing episodes in the outer liquid layers that take place upon crystallization (see [Renado et al. 2010](#)). In particular, during the crystallization process, the oxygen abundance in the crystallizing region increases, and the overlying liquid mantle becomes carbon-enriched as a result of mixing induced by a Rayleigh-Taylor instability at the region above the crystallized core. Once the crystallization process is completed, the chemical profiles of all the elements become frozen, including that of  $^{22}\text{Ne}$ .

### 3. Delayed detonations of Chandrasekhar-mass white dwarfs

Here we report the results of the explosion of a massive white dwarf using the chemical profiles obtained at the beginning and

the end of the cooling process. The pre-supernova model is a cool, isothermal, Chandrasekhar-mass white dwarf built in hydrostatic equilibrium with a central density  $\rho_c = 3 \times 10^9 \text{ g cm}^{-3}$ . The central  $1 M_{\odot}$  has the same chemical composition as the carbon-oxygen core obtained in the cooling sequences, while the composition of the envelope of mass  $M_{\text{Ch}} - 1 M_{\odot}$  is the same as that of the outermost shell of the carbon-oxygen core. As we wish to maximize the impact of the chemical profiles on the supernova outcome, we do not take into account here convective mixing during the pre-supernova carbon simmering phase.

The present models are based on the delayed-detonation (DDT) paradigm ([Khokhlov 1991](#)), in which thermonuclear combustion initially proceeds through a subsonic deflagration until it makes a transition to a supersonic detonation wave. The location of the deflagration-detonation transition is usually parametrized by its density,  $\rho_{\text{DDT}}$ . The supernova hydrodynamics and nucleosynthetic (post-processing) codes we use are the same as in [Bravo et al. \(1996\)](#) and [Badenes et al. \(2003\)](#). We sketch here, for completeness, the method used by the hydrodynamics code to simulate DDT models and calculate the nuclear energy generation rate. In the DDT models, the flame propagates initially as a deflagration, with a velocity fixed at a constant fraction, 3%, of the local sound velocity. When the flame density *ahead* of the flame reaches the prescribed transition density,  $\rho_{\text{DDT}}$ , the flame front is accelerated artificially to a large fraction of the sound speed, resulting in the subsequent formation of a detonation. Changes in the chemical composition are followed during the propagation of the burning front in the deflagration and detonation modes using an  $\alpha$ -network from  $^4\text{He}$  to  $^{28}\text{Si}$  plus the conversion of  $^{28}\text{Si}$  to  $^{56}\text{Ni}$  in a single step. When the temperature of a mass shell exceeds  $5.5 \times 10^9 \text{ K}$ , nuclear statistical equilibrium (NSE) is assumed. Once attained, NSE is maintained as long as the temperature remains above  $2 \times 10^9 \text{ K}$ , providing a nuclear energy generation rate accurate enough for the hydrodynamical simulations. Weak interactions during NSE determine the evolution of the electron mole number,  $Y_e$ ,

$$\frac{dY_e}{dt} = \sum_i \lambda_i Y_i, \quad (1)$$

where  $\lambda_i$ , accounting for all kind of weak interactions, and the molar fractions,  $Y_i$ , are set by the NSE equations. The final nucleosynthesis was computed separately with the nuclear reaction network described by [Bravo et al. \(1993\)](#), with updated reaction rates taken from the REACLIB compilation ([Rauscher & Thielemann 2000](#)), using the temperature and densities of each mass zone provided by the hydrocode.

Bolometric light curves were obtained by means of the code described in [Bravo et al. \(1993, 1996\)](#). In general, the bolometric light curves obtained with this code during the pre-maximum and maximum phases are in fairly good agreement with those computed by directly solving the radiative transfer equations (see [Höflich et al. 1993](#)).

Table 1 gives details of the models we have computed so far. Each model is characterized by two parameters: its cooling time (age), and the deflagration-detonation transition density,  $\rho_{\text{DDT}}$ . This density is the main unknown in the DDT SNIa models. In one-dimensional calculations such as those reported here,  $\rho_{\text{DDT}}$  is usually a free parameter. While multi-dimensional SNIa models may be able to emulate the physical dependences of  $\rho_{\text{DDT}}$ , in principle, state-of-the-art models are still nowadays not able to do it (for a recent attempt in this direction see, e.g. [Jackson et al. 2010](#)). Thus, we repeated the simulations for several values of  $\rho_{\text{DDT}}$ , as shown in Table 1. In some calculations, we used initial models resulting from using a diffusion coefficient of  $^{22}\text{Ne}$

**Table 1.** Results of Chandrasekhar-mass explosions.

| Age <sup>a</sup><br>(Gyr) | $\rho_{\text{DDT}}$<br>( $\text{g cm}^{-3}$ ) | $M(^{56}\text{Ni})$<br>( $M_{\odot}$ ) | $M(\text{IME})^b$<br>( $M_{\odot}$ ) | $K^c$<br>( $10^{51}$ erg) | $m_{\text{max}}^d$<br>(mag) |
|---------------------------|---|--|--------------------------------------|---------------------------|-----------------------------|
| 0.6                       | $1.6 \times 10^7$                             | 0.40                                   | 0.67                                 | 1.26                      | -18.78                      |
| 8.0                       | $1.6 \times 10^7$                             | 0.43                                   | 0.70                                 | 1.37                      | -18.84                      |
| 1.0 <sup>e</sup>          | $1.6 \times 10^7$                             | 0.41                                   | 0.67                                 | 1.27                      | -18.79                      |
| 9.6 <sup>e</sup>          | $1.6 \times 10^7$                             | 0.43                                   | 0.69                                 | 1.38                      | -18.88                      |
| 1.0 <sup>e</sup>          | $3.0 \times 10^7$                             | 0.71                                   | 0.42                                 | 1.42                      | -19.45                      |
| 9.6 <sup>e</sup>          | $3.0 \times 10^7$                             | 0.74                                   | 0.42                                 | 1.51                      | -19.50                      |
| 0.6                       | $2.4 \times 10^7$ <sup>f</sup>                | 0.59                                   | 0.52                                 | 1.37                      | -19.23                      |
| 8.0                       | $3.7 \times 10^7$ <sup>g</sup>                | 0.83                                   | 0.34                                 | 1.54                      | -19.63                      |

**Notes.** All models: central density,  $\rho_c = 3.0 \times 10^9$   $\text{g cm}^{-3}$ .

(<sup>a</sup>) Time since the beginning of the cooling sequence. (<sup>b</sup>) Synthesized mass of intermediate-mass elements, from Si to Ca. (<sup>c</sup>) Kinetic energy of the ejecta. (<sup>d</sup>) Bolometric magnitude at maximum. (<sup>e</sup>) Model with the diffusion coefficient of  $^{22}\text{Ne}$  increased by a factor 5. (<sup>f</sup>) Deflagration-to-detonation transition density estimated from the chemical composition at the flame front (Eq. (2)):  $X(^{12}\text{C}) = 0.36$ ,  $X(^{22}\text{Ne}) = 0.020$ . (<sup>g</sup>) Deflagration-to-detonation transition density estimated from the chemical composition at the flame front using Eq. (2):  $X(^{12}\text{C}) = 0.24$ ,  $X(^{22}\text{Ne}) = 0.022$ .

during white dwarf cooling artificially increased by a factor of five. For each combination of  $\rho_{\text{DDT}}$  and diffusion coefficient, we computed two models, one belonging to the beginning of crystallization of the white dwarf (“young” model) and another at an advanced state of crystallization (~95–96%, “old” model).

### 3.1. Detonating at a fixed $\rho_{\text{DDT}}$

The first two rows of Table 1 give the mass of radioactive  $^{56}\text{Ni}$ , the mass of intermediate-mass elements (IME, mostly composed of Si and S), the kinetic energy of the ejecta, and the bolometric magnitude of the supernova at maximum, for two models computed at the beginning and the end of the white dwarf cooling sequence, with  $\rho_{\text{DDT}} = 1.6 \times 10^7$   $\text{g cm}^{-3}$ . The results are quite insensitive to the age of the pre-supernova, the difference in brightnesses being ~0.06 mag. The differences in both the yield of IMEs and the kinetic energy are correspondingly small, on the order of 5% and 9%, respectively.

#### 3.1.1. Enhanced diffusion of $^{22}\text{Ne}$

The third and fourth rows of Table 1 give the results of models identical to the ones just discussed but for the enhanced diffusion coefficient of  $^{22}\text{Ne}$  during white dwarf cooling. The results are nearly identical to those obtained with the nominal diffusion coefficient. Thus, any uncertainty in the diffusion coefficient does not translate into appreciable differences in the observational properties of SNIa. These conclusions are independent of the value of  $\rho_{\text{DDT}}$  used in the supernova calculations, as can be seen in the next two rows where we show the results for  $\rho_{\text{DDT}} = 3.0 \times 10^7$   $\text{g cm}^{-3}$ .

Figures 3 and 4 show the final chemical composition of the ejecta as a function of the ejecta mass (as a Lagrangian coordinate), for the two models with enhanced diffusion coefficient and  $\rho_{\text{DDT}} = 1.6 \times 10^7$   $\text{g cm}^{-3}$ . The main difference between the initial models (see Fig. 2) lies in the concentration of  $^{22}\text{Ne}$  in the central  $0.6 M_{\odot}$ , which leads to a larger  $^{22}\text{Ne}$  mass fraction (~50%) in the oldest model. However, the chemical profiles of the ejecta of both models are nearly the same below this Lagrangian mass.

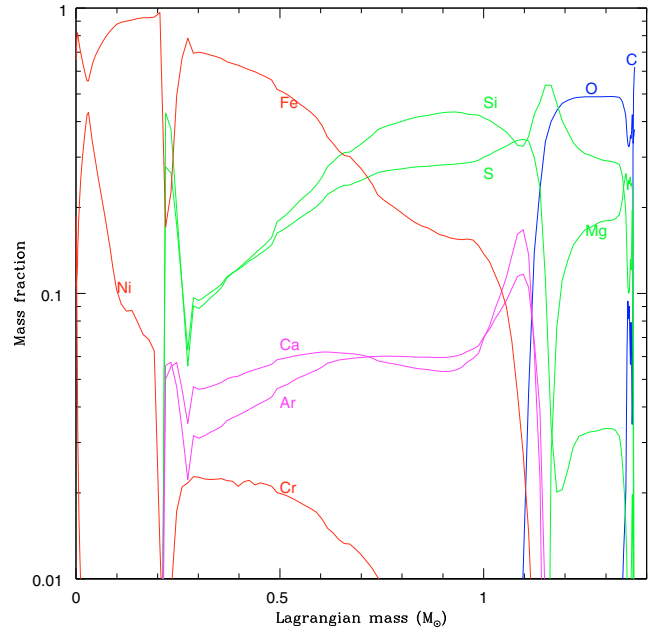


**Fig. 3.** Final chemical composition of the ejecta for the model detonated at the beginning of the cooling process with a fixed  $\rho_{\text{DDT}} = 1.6 \times 10^7$   $\text{g cm}^{-3}$  and enhanced diffusion. The abundances shown reflect the elemental composition after radioactive disintegrations. See the online edition of the journal for a color version of the figure.

Between ~0.6  $M_{\odot}$  and 1  $M_{\odot}$ , the oldest model (8.0 Gyr age) has slightly larger mass fractions of Si and S and less Fe and Cr, although the differences are quite modest. The reason for these differences is the following. As the thermonuclear wave propagates through the central regions of the white dwarf, it completely incinerates the material up to a composition in nuclear statistical equilibrium. The oldest model having a larger central neutron excess (larger  $^{22}\text{Ne}$  mass fraction) releases less energy during the incineration of carbon and oxygen in reaching NSE, which causes a slightly slower expansion during the initial phases of the explosion, and higher densities at the position of the flame. As a consequence, the subsequent combustion of the layers above a ~0.6  $M_{\odot}$  Lagrangian mass is able to reach a more advanced combustion stage than if the expansion had been faster (as in the youngest model, of 0.6 Gyr age), and more Fe and less IMEs are produced in these layers.

### 3.2. Transition density function of the chemical composition

We now speculate whether  $\rho_{\text{DDT}}$  is a function of the local chemical composition (Chamulak et al. 2007; Woosley 2007; Bravo et al. 2010; Jackson et al. 2010)<sup>1</sup>. In considering this scenario, we scaled the transition density as a function of the local chemical composition as (see Bravo et al. 2010, for details)

$$\rho_{\text{DDT}} \propto X(^{12}\text{C})^{-1.3} (1 + 129\eta)^{-0.6}, \quad (2)$$

where the neutron excess,  $\eta = 1 - 2Y_e$ , is related to the  $^{22}\text{Ne}$  mass fraction by

$$\eta = \frac{X(^{22}\text{Ne})}{11}. \quad (3)$$

<sup>1</sup> The models discussed in this section are based on the nominal value of the diffusion coefficient.

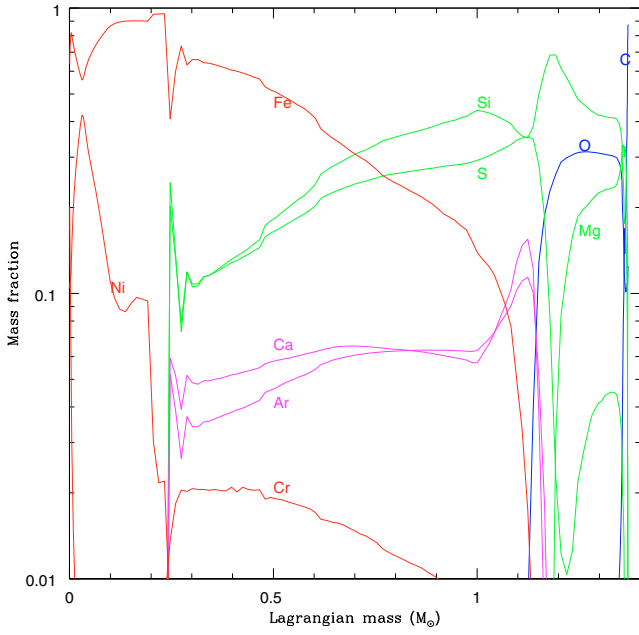


**Fig. 4.** Same as Fig. 3, but at the end of the crystallization phase.

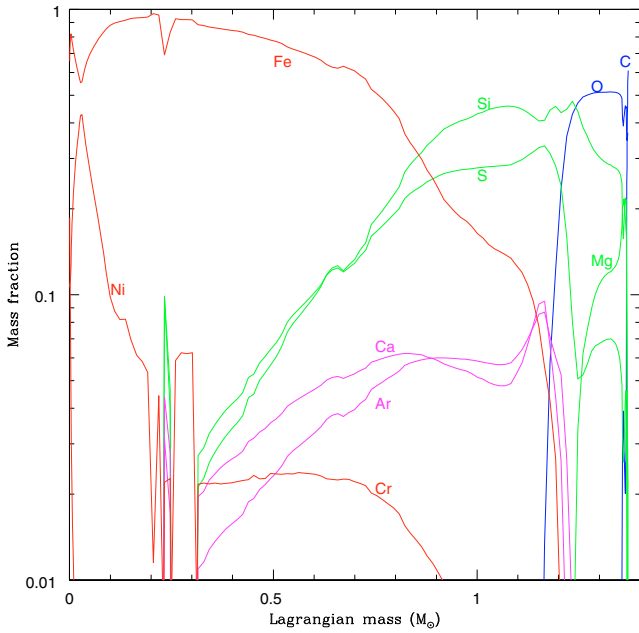


**Fig. 5.** Chemical composition of the ejecta for the model with  $\rho_{\text{DDT}}$  function of the mass fractions of  $^{12}\text{C}$  and  $^{22}\text{Ne}$  as given by Eq. (2) at the beginning of the cooling process:  $X(^{12}\text{C}) = 0.36$ ,  $X(^{22}\text{Ne}) = 0.020$  (see Table 1).

Equation (2) implies that a reduction in the carbon mass fraction translates into a higher  $\rho_{\text{DDT}}$ , while an increase in the  $^{22}\text{Ne}$  mass fraction has the opposite effect. The results we obtained are given in the last two rows of Table 1, and in Figs. 5 and 6, where the final chemical composition of the ejecta is shown for the models corresponding to both the beginning and the end of the white dwarf cooling process.

Allowing  $\rho_{\text{DDT}}$  to be a function of the local (at the position of the flame front) chemical composition makes a great difference.

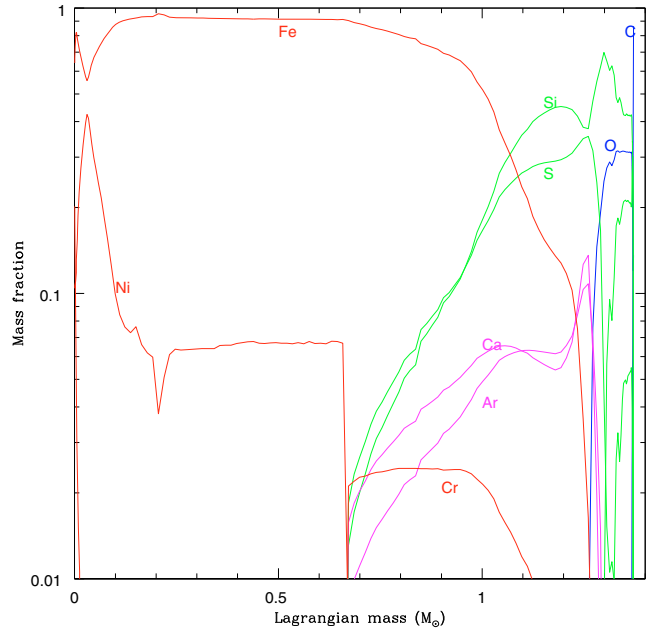


**Fig. 6.** Chemical composition of the ejecta for the model with  $\rho_{\text{DDT}}$  function of the mass fractions of  $^{12}\text{C}$  and  $^{22}\text{Ne}$  as given by Eq. (2) at the end of the crystallization phase:  $X(^{12}\text{C}) = 0.24$ ,  $X(^{22}\text{Ne}) = 0.022$  (see Table 1).

The transition from deflagration to detonation takes place at a Lagrangian mass  $\sim 0.22 M_{\odot}$ <sup>2</sup>. The abundances of  $^{12}\text{C}$  and  $^{22}\text{Ne}$  at this location are 0.36 and 0.020, respectively, for the youngest model, and 0.24 and 0.022 for the oldest model (see Fig. 1). The main effect comes from the reduction in the carbon mass fraction with age, which causes an increase of  $\sim 63\%$  in  $\rho_{\text{DDT}}$ . The modest variation in the neon abundance at the flame front only makes the transition density decrease by  $\sim 1\%$ . Finally, the difference in  $\rho_{\text{DDT}}$  as a function of the progenitor age translates into a SNIa brightness difference of 0.40 mag.

In these calculations, the production of IMEs by SNIa is strongly affected by the age of the progenitor, since it is reduced by a factor of  $\sim 0.65$  for the oldest model. As can be seen in Figs. 5 and 6, the larger  $\rho_{\text{DDT}}$  is, the more extended the Fe production region and the more squeezed the region rich in IMEs is.

#### 4. Explosion of sub-Chandrasekhar white dwarfs

The sub-Chandrasekhar model of SNIa (Woosley et al. 1980; Nomoto 1982; Woosley et al. 1986; Iben & Tutukov 1991; Limongi & Tornambe 1991; Livne & Glasner 1991; Woosley & Weaver 1994; García-Senz et al. 1999) was challenged 14 years ago because its spectra was excessively blue compared to SNIa observations (Höflich & Khokhlov 1996). This disagreement had its origin in the assumption that a thick helium layer was necessary to detonate a sub-Chandrasekhar white dwarf. However, there has been renewed interest in this kind of explosion because of the possibility that they produce a new class of underluminous supernovae (Bildsten et al. 2007), and the finding that a white dwarf detonation is possible for lower helium shell

<sup>2</sup> The location of the DDT can be identified in Figs. 3 to 6 with the sudden drop in the Ni profile slightly above  $0.2 M_{\odot}$ . This discontinuity is a numerical artifact of the procedure used to transmute a deflagration front into a detonation wave.

**Table 2.** Results of sub-Chandrasekhar explosions.

| Age <sup>a</sup><br>(Gyr) | $h_{\text{ig}}^b$<br>(km) | $M(^{56}\text{Ni})$<br>( $M_{\odot}$ ) | $M(\text{Fe, sta})^c$<br>( $M_{\odot}$ ) | $M(\text{IME})$<br>( $M_{\odot}$ ) | $K$<br>( $10^{51}$ erg) |
|---------------------------|---------------------------|--|--|------------------------------------|-------------------------|
| <sup>d</sup> –            | 0                         | 0.70                                   | 0.055                                    | 0.22                               | 1.39                    |
| 0.6                       | 0                         | 0.69                                   | 0.054                                    | 0.23                               | 1.34                    |
| 8.0                       | 0                         | 0.68                                   | 0.058                                    | 0.24                               | 1.35                    |
| 0.6                       | 70                        | 0.63                                   | 0.054                                    | 0.28                               | 1.31                    |
| 8.0                       | 70                        | 0.64                                   | 0.057                                    | 0.30                               | 1.34                    |

**Notes.** All models: mass of the carbon-oxygen core,  $M_{\text{core}} = 1 M_{\odot}$ ; mass of the He envelope  $M_{\text{env}} = 0.080 M_{\odot}$ ; central density,  $\rho_c = 5.8 \times 10^7 \text{ g cm}^{-3}$ ; density at the base of the He envelope,  $\rho_{\text{base}} = 2.1 \times 10^6 \text{ g cm}^{-3}$ .

<sup>(a)</sup> Time since the beginning of the cooling sequence. <sup>(b)</sup> Altitude at which the He detonation starts. <sup>(c)</sup> Ejected mass of *stable* Fe-group nuclei. <sup>(d)</sup> Reference model, with a homogeneous composition of the core of 49% carbon and oxygen plus 2%  $^{22}\text{Ne}$ .

masses than previously thought (Fink et al. 2010). This last point allows a better agreement with SNIa optical properties (Kromer et al. 2010) but the models still show some deficiencies, particularly in terms of their lack of a central region rich in stable Fe-group elements, as demanded by infrared observations of SNIa (Höflich et al. 2004). One possible solution for this deficiency, proposed by Kromer et al. (2010), might be a higher neutron excess in the central regions of the white dwarf caused by gravitational settling of  $^{22}\text{Ne}$  during white dwarf cooling. We test this hypothesis in the following.

The initial models used in our sub-Chandrasekhar explosion calculations are composed of a carbon-oxygen core and a helium envelope. The core has the same chemical structure as the carbon-oxygen core in the  $1 M_{\odot}$  white dwarf evolved with the LPCODE code (Sect. 2), taken at different ages since the beginning of the cooling process. The envelope has a mass of  $0.080 M_{\odot}$  and is composed of 100% He. The mechanical structure of the white dwarf that resulted from the cooling sequences was readjusted to reestablish the hydrostatic equilibrium taking into account the envelope. As a result, the central density changed from  $\sim 3.5 \times 10^7 \text{ g cm}^{-3}$ , as given by the cooling sequences, to  $\sim 5.8 \times 10^7 \text{ g cm}^{-3}$  in our initial models. The density at the base of the He envelope was  $\sim 2.1 \times 10^6 \text{ g cm}^{-3}$ .

The models we computed are summarized in Table 2. The models were calculated at two different ages of the progenitor white dwarf, and the initial He detonation was started at two different locations: just at the base of the helium envelope, and at an altitude of 70 km above this. We also computed a reference model in which the composition of the core is uniform and has equal mass fractions of carbon and oxygen (first row in Table 2).

The precise point at which He detonates is not known with precision because of unresolved convective motions during the first stages of He burning at the base of the envelope, so the above procedure allows us to evaluate the impact of the chemical differentiation of the white dwarf in two extreme conditions. Detonating helium at different altitudes can have consequences for the outcome of the inward shock wave that is launched into the white dwarf core (Livne & Glasner 1991). If He ignition occurs at a high enough altitude above the core, the He detonation wave has time to develop well before it arrives at the core and it can be strong enough then to directly induce an inwardly moving carbon detonation. This possibility depends as well on the carbon mass fraction at the outermost part of the core, which in turn depends on the age of the progenitor white dwarf.

**Table 3.** Induced detonation of carbon.

| $\rho$<br>( $\text{g cm}^{-3}$ ) | $X(^{12}\text{C})^a$ | Altitude <sup>b</sup><br>(km) | Detonation? |
|----------------------------------|----------------------|-------------------------------|-------------|
| $6 \times 10^6$                  | 0.50                 | 5                             | no          |
| $6 \times 10^6$                  | 0.61                 | 5                             | no          |
| $6 \times 10^6$                  | 0.86                 | 5                             | yes         |
| $6 \times 10^6$                  | 0.50                 | 10                            | weak        |
| $6 \times 10^6$                  | 0.61                 | 10                            | yes         |
| $6 \times 10^6$                  | 0.86                 | 10                            | yes         |
| $6 \times 10^6$                  | 0.50                 | 20                            | yes         |
| $2 \times 10^6$                  | 0.50                 | 50                            | no          |
| $2 \times 10^6$                  | 0.61                 | 50                            | no          |
| $2 \times 10^6$                  | 0.86                 | 50                            | no          |
| $2 \times 10^6$                  | 0.50                 | 100                           | no          |
| $2 \times 10^6$                  | 0.61                 | 100                           | weak        |
| $2 \times 10^6$                  | 0.86                 | 100                           | weak        |
| $2 \times 10^6$                  | 0.50                 | 200                           | weak        |
| $2 \times 10^6$                  | 0.61                 | 200                           | weak        |
| $2 \times 10^6$                  | 0.86                 | 200                           | weak        |

**Notes.** <sup>(a)</sup> Carbon mass fraction surrounding the central He ball. In all calculations, the oxygen mass fraction in this region was set to  $X(^{16}\text{O}) = 1 - X(^{12}\text{C})$ . <sup>(b)</sup> Radius of the central ball made of 99%  $^4\text{He}$  and 1%  $^{12}\text{C}$ .

#### 4.1. Edge-lit detonation of carbon

We explored the conditions for the formation of a stable self-sustained carbon detonation induced by a He detonation, as a function of the carbon mass fraction and the altitude at which He is ignited. A similar analysis was performed by García-Senz et al. (1999), but they explored a range of  $^{12}\text{C}$  mass fractions below 0.5, while those we are interested in are much larger ( $X(^{12}\text{C}) = 0.61$  in our young progenitor model, and  $X(^{12}\text{C}) = 0.86$  in the old progenitor model). García-Senz et al. (1999) found that the probability of a self-sustained detonation occurring in the core is very sensitive to the carbon mass fraction.

In the present numerical experiments, we applied the same methodology adopted in Bravo & García-Senz (2009, and references therein). We followed the hydrodynamical and nuclear evolution of an isothermal uniform density sphere consisting of a central ball made of 99%  $^4\text{He}$  and 1%  $^{12}\text{C}$ , surrounded by a much higher mass of the same chemical composition as the outermost layer of the carbon-oxygen core of the white dwarf, produced by the cooling sequences. The radius of the central ball plays the role of the altitude at which He ignites in the sub-Chandrasekhar models. The He detonation was started by incinerating a central region containing between 1% and 8% of the mass of the central helium-rich ball.

The results of these numerical experiments are summarized in Table 3, where we have investigated the induction of carbon detonation at two densities:  $2 \times 10^6 \text{ g cm}^{-3}$ , which matches the density at the base of the helium envelope in our  $1.080 M_{\odot}$  sub-Chandrasekhar models, and  $6 \times 10^6 \text{ g cm}^{-3}$ , which would be representative of models with a higher total mass. Here, a “weak detonation” means a carbon detonation in which the temperature is not high enough to burn oxygen directly (see García-Senz et al. 1999). In a sub-Chandrasekhar explosion, such an edge-lit weak detonation will strengthen as it moves into denser regions, reaching increasingly higher temperatures and allowing the completion of burning sequences from explosive oxygen burning until NSE. The successful launching of a carbon detonation wave is found to depend strongly on the

density and the altitude of He ignition, and weakly on the carbon mass fraction. For instance, for a density of  $2 \times 10^6 \text{ g cm}^{-3}$ , the minimum altitude at which a carbon detonation develops in our simulations is 200 km for a composition of 50%:50% carbon and oxygen, and only 100 km for the two compositions richer in carbon that we explored. For the highest density we used,  $6 \times 10^6 \text{ g cm}^{-3}$ , and an altitude of 5 km, a carbon detonation was obtained only for the largest carbon mass fraction,  $X(^{12}\text{C}) = 0.81$ . Thus, the age of the progenitor system can determine the kind of dynamical event following He ignition in a sub-Chandrasekhar white dwarf, i.e. either a central carbon detonation or a shell carbon detonation.

#### 4.2. Explosion models

The effects of white dwarf crystallization and  $^{22}\text{Ne}$  sedimentation on sub-Chandrasekhar explosions can be seen in Table 2. First, comparing the three models that ignited He at the base of the envelope (first three rows, with  $h_{\text{ig}} = 0$ ) we see that the impact of chemical differentiation is minimum, on the order of a few percent in  $^{56}\text{Ni}$  and IMEs yields and in the kinetic energy. Second, comparing the two models with  $h_{\text{ig}} = 70 \text{ km}$ , we observe the same lack of dependence of the outcome of the explosion on the age of the progenitor system.

A further comparison can be established between a young model in which the edge-lit detonation of carbon fails (and, later, carbon detonates at the center of the white dwarf), and an old model in which the edge-lit detonation of carbon is successful. Figures 7 (young model, second row in Table 2) and 8 (old model, last row in Table 2) show the evolution of the white dwarf in both cases. Even though the history of the explosion is quite sensitive to the location of carbon detonation, the final result is not so different. In the last panel of Figs. 7 and 8, we show the final mechanical, thermal, and velocity profiles of the ejecta, together with the profile of the mass fraction of stable Fe-group elements (red dotted line). The concentration of stable Fe-group elements is clearly insensitive to the age of the progenitor system of the exploding sub-Chandrasekhar white dwarf.

### 5. Conclusions

We have investigated the sensitivity of SNIa energetics and nucleosynthesis to realistic chemical profiles based on white dwarf cooling sequences calculated by Althaus et al. (2010). The cooling sequences provide a link between the white dwarf chemical structure and the age of the supernova progenitor system. Neither gravitational settling of  $^{22}\text{Ne}$  nor chemical differentiation of  $^{12}\text{C}$  and  $^{16}\text{O}$  during white dwarf crystallization have a sizable impact on the properties of SNIa, unless there is a direct dependence of the flame properties on chemical abundances. If the density of transition from deflagration to detonation in SNIa did not depend on the chemical composition, the variation in the supernova magnitude with age produced by chemical differentiation would be as small as  $\sim 0.06 \text{ mag}$  for an age difference of  $\sim 7.4 \text{ Gyr}$ . We emphasize that these results have been obtained by neglecting mixing during the pre-supernova carbon simmering phase. If this mixing process is efficient, it will erase any trace of the chemical separation achieved during white dwarf cooling, thus the chemical separation will leave no imprint on the supernova properties. Our results therefore represent the maximum possible effect that can be expected from the gravitational settling of  $^{22}\text{Ne}$  and  $^{16}\text{O}$ .

If the density of transition from deflagration to detonation in SNIa is a function of the chemical composition, and if we

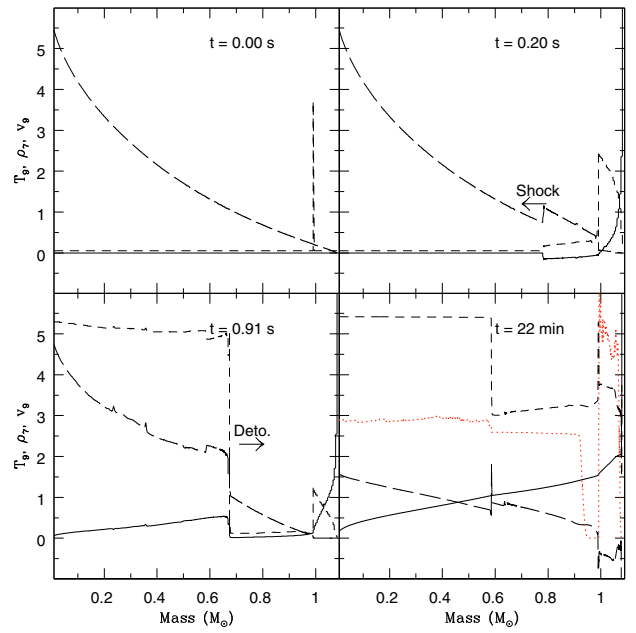


**Fig. 7.** Development of the detonation of a sub-Chandrasekhar mass white dwarf that explodes at the beginning of the cooling process. From left to right and top to bottom, the first three panels show the profiles of temperature in units of  $10^9 \text{ K}$  (short-dashed line), density in units of  $10^7 \text{ g cm}^{-3}$  (long-dashed line), and velocity in units of  $10000 \text{ km s}^{-1}$  (solid line), at three times since the beginning of He detonation. In this model, the He detonated at the base of the envelope, so it was unable to produce an edge-lit detonation of carbon (see Tables 2 and 3). Instead, an initially weak inwardly moving shock traveled through the white dwarf (second panel). Shortly before reaching the center, the shock strengthened enough to produce a carbon detonation that traveled outwards processing most of the matter on top (third panel). The last panel shows the final profiles of  $\log(T)$  (short-dashed line),  $\log(10^3 \rho)$  (long-dashed line), velocity (solid line), and  $50X(\text{Fe, stable})$ , where  $X(\text{Fe, stable})$  is the mass fraction of stable Fe-group nuclei (red dotted line). The discontinuity in the thermal profile in the last panel is due to the local deposition of the photons emitted in the radioactive disintegration of  $^{56}\text{Ni}$ .

neglect convective mixing during the pre-supernova carbon simmering phase, the difference in maximum magnitude between a white dwarf exploding at the beginning of the cooling process and another one that has experienced substantial crystallization can be as large as  $\sim 0.4 \text{ mag}$ . For this variation in magnitude to take place, it suffices that the central part of the white dwarf has crystallized (22% in mass in our models), so that the transition from deflagration to detonation takes place in a region that has been depleted in carbon. For a  $1 M_{\odot}$  white dwarf, the crystallization of the central 22% in mass occurs at an age of only 1.25 Gyr.

The physics of  $^{22}\text{Ne}$  sedimentation is nowadays sufficiently well-known that the calculations presented in this paper cannot experience much variation. We have also explored the impact of using an unrealistically large diffusion coefficient, which nevertheless had a very small impact on the observable properties of SNIa explosions. We stress that to obtain a large concentration of  $^{22}\text{Ne}$  in the central layers of a white dwarf the star would have to be made of pure carbon, which is not applicable in the more general case of carbon-oxygen white dwarfs. Thus, our results concerning the lack of imprint of the  $^{22}\text{Ne}$  sedimentation on SNIa are quite robust.

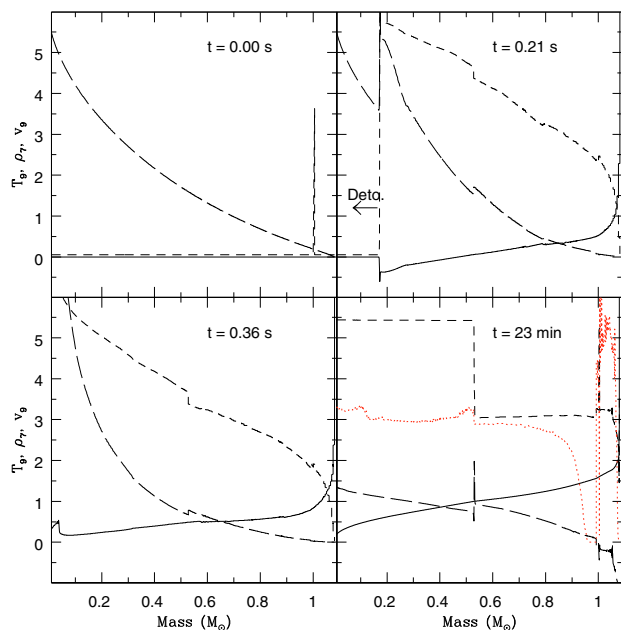


**Fig. 8.** Development of the detonation of a sub-Chandrasekhar mass white dwarf that explodes at the end of the crystallization phase. The meaning of the different curves is the same as in Fig. 7. In this model, the He detonated at an altitude of 70 km from the base of the envelope, and launched a second inwardly moving carbon detonation (see Tables 2 and 3), as can be seen already in the second panel. The carbon detonation processed all the matter down to the center of the white dwarf and, thereafter, sent a weak shock wave outwards (visible in the third panel) at a Lagrangian mass of  $\sim 0.5 M_{\odot}$ .

In the light of the present results, the only possible ways in which chemical differentiation might affect the thermonuclear explosion of a white dwarf are either through a composition dependent density of transition from a deflagration to a detonation, or through composition dependent thermonuclear runaway conditions (usually taken to be the initial conditions for SNIa simulations). Linking explosion models to the last stages of white dwarf evolution remains one of the main challenges of SNIa theory.

Finally, we highlight the importance of developing realistic pre-supernova evolutionary calculations to understand the constraints imposed by observations on SNIa models. In the case of sub-Chandrasekhar explosions, we have proven that the sedimentation of  $^{22}\text{Ne}$  does not efficiently increase the neutron excess in the central region of the white dwarf prior to the explosive event. Thus, this sedimentation cannot be responsible for the production of the stable Fe-rich core inferred from observations of SNIa. However, the crystallization of the white dwarf entails an increase in the carbon abundance in the outermost layers of the carbon-oxygen white dwarf core, which may have consequences for the formation of a double detonation (outwards in He-rich matter, inwards in the C-O core) following helium ignition close to the base of the helium mantle.

*Acknowledgements.* This work was partially supported by the AGAUR, by MCINN grant AYA2008-04211-C02, by the European Union FEDER funds, by AGENCIA: Programa de Modernización Tecnológica BID 1728/OC-AR, and by PIP 2008-00940 from CONICET. LGA also acknowledges a PIV grant of the AGAUR of the Generalitat de Catalunya.

## References

- Althaus, L. G., García-Berro, E., Renedo, I., et al. 2010, ApJ, accepted  
 Badenes, C., Bravo, E., Borkowski, K. J., & Domínguez, I. 2003, ApJ, 593, 358  
 Bildsten, L., & Hall, D. M. 2001, ApJ, 549, L219  
 Bildsten, L., Shen, K. J., Weinberg, N. N., & Nelemans, G. 2007, ApJ, 662, L95  
 Branch, D., Livio, M., Yungelson, L. R., Boffi, F. R., & Baron, E. 1995, PASP, 107, 1019  
 Bravo, E., & García-Senz, D. 2009, ApJ, 695, 1244  
 Bravo, E., Isern, J., Canal, R., & Labay, J. 1992, A&A, 257, 534  
 Bravo, E., Domínguez, I., Isern, J., et al. 1993, A&A, 269, 187  
 Bravo, E., Tornambe, A., Domínguez, I., & Isern, J. 1996, A&A, 306, 811  
 Bravo, E., Domínguez, I., Badenes, C., Piersanti, L., & Straniero, O. 2010, ApJ, 711, L66  
 Chamulak, D. A., Brown, E. F., & Timmes, F. X. 2007, ApJ, 655, L93  
 Deloye, C. J., & Bildsten, L. 2002, ApJ, 580, 1077  
 Fink, M., Röpke, F. K., Hillebrandt, W., et al. 2010, A&A, 514, A53  
 Gallagher, J. S., Garnavich, P. M., Caldwell, N., et al. 2008, ApJ, 685, 752  
 García-Berro, E., Althaus, L. G., Córscico, A. H., & Isern, J. 2008, ApJ, 677, 473  
 García-Berro, E., Torres, S., Althaus, L. G., et al. 2010, Nature, 465, 194  
 García-Senz, D., Bravo, E., & Woosley, S. E. 1999, A&A, 349, 177  
 Hamuy, M., Phillips, M. M., Suntzeff, N. B., et al. 1996, AJ, 112, 2408  
 Hamuy, M., Trager, S. C., Pinto, P. A., et al. 2000, AJ, 120, 1479  
 Hillebrandt, W., & Niemeyer, J. C. 2000, ARA&A, 38, 191  
 Höflich, P., & Khokhlov, A. 1996, ApJ, 457, 500  
 Höflich, P., Mueller, E., & Khokhlov, A. 1993, A&A, 268, 570  
 Höflich, P., Gerardy, C. L., Nomoto, K., et al. 2004, ApJ, 617, 1258  
 Howell, D. A., Sullivan, M., Brown, E. F., et al. 2009, ApJ, 691, 661  
 Hoyle, F., & Fowler, W. A. 1960, ApJ, 132, 565  
 Iben, Jr., I., & Tutukov, A. V. 1991, ApJ, 370, 615  
 Jackson, A. P., Calder, A. C., Townsley, D. M., et al. 2010, ApJ, 720, 99  
 Khokhlov, A. M. 1991, A&A, 245, 114  
 Kromer, M., Sim, S. A., Fink, M., et al. 2010, ApJ, 719, 1067  
 Krueger, B. K., Jackson, A. P., Townsley, D. M., et al. 2010, ApJ, 719, L5  
 Limongi, M., & Tornambe, A. 1991, ApJ, 371, 317  
 Livne, E., & Glasner, A. S. 1991, ApJ, 370, 272  
 Neill, J. D., Sullivan, M., Howell, D. A., et al. 2009, ApJ, 707, 1449  
 Nomoto, K. 1982, ApJ, 257, 780  
 Nomoto, K., Umeda, H., Hachisu, I., et al. 2000, in Type Ia Supernovae, Theory and Cosmology, ed. J. C. Niemeyer, & J. W. Truran, 63  
 Perets, H. B., Gal-Yam, A., Mazzali, P. A., et al. 2010, Nature, 465, 322  
 Perlmutter, S., Aldering, G., Goldhaber, G., et al. 1999, ApJ, 517, 565  
 Piro, A. L., & Bildsten, L. 2008, ApJ, 673, 1009  
 Piro, A. L., & Chang, P. 2008, ApJ, 678, 1158  
 Rauscher, T., & Thielemann, F. 2000, Atomic Data and Nuclear Data Tables, 75, 1  
 Renedo, I., Althaus, L. G., Miller Bertolami, M. M., et al. 2010, ApJ, 717, 183  
 Riess, A. G., Filippenko, A. V., Challis, P., et al. 1998, AJ, 116, 1009  
 Röpke, F. K. 2006, ed. S. Roeser, Rev. Mod. Astron., 19, 127  
 Sim, S. A., Röpke, F. K., Hillebrandt, W., et al. 2010, ApJ, 714, L52  
 Timmes, F. X., Brown, E. F., & Truran, J. W. 2003, ApJ, 590, L83  
 Tonry, J. L. 2005, Physica Scripta Volume T, 117, 11  
 Wang, X., Wang, L., Pain, R., Zhou, X., & Li, Z. 2006, ApJ, 645, 488  
 Woosley, S. E. 2007, ApJ, 668, 1109  
 Woosley, S. E., & Weaver, T. A. 1994, ApJ, 423, 371  
 Woosley, S. E., Weaver, T. A., & Taam, R. E. 1980, in Texas Workshop on type I Supernovae, ed. J. C. Wheeler, 96  
 Woosley, S. E., Taam, R. E., & Weaver, T. A. 1986, ApJ, 301, 601